Journal of The Electrochemical Society, 2022 **169** 040504
1945-7111/2022/169(4)/040504/9/$40.00 © 2022 The Electrochemical Society ("ECS"). Published on behalf of ECS by IOP Publishing Limited

Disrupting Sodium Ordering and Phase Transitions in a Layered Oxide Cathode

Nicholas S. Grundish,[1] Hailong Lyu,[1] Ieuan D. Seymour,[2,3] Graeme Henkelman,[3] and Hadi Khani[1,z]

[1]*Materials Science and Engineering Program and Texas Materials Institute, The University of Texas at Austin, Austin, Texas 78712, United States of America*
[2]*Department of Materials, Imperial College London, London, SW72AZ, United Kingdom*
[3]*Department of Chemistry and the Oden Institute for Computational Engineering and Sciences, The University of Texas at Austin, Austin, Texas 78712, United States of America*

Layered Na_xMO_2 cathodes are of immense interest as rechargeable sodium batteries further their development as a lithium-ion battery alternative. However, two primary intrinsic structural issues hinder their practicality—sodium ordering and transition-metal layer gliding during cycling. These phenomena plague the electrochemical profiles of these materials with several unwanted voltage plateaus. A Na^+ and Fe^{3+} substitution for Ni^{2+} strategy is employed here to obtain a series of $Na_{3+x}Ni_{2-2x}Fe_xSbO_6$ ($0 \leqslant x \leqslant 0.5$) materials to suppress the structural phenomena that are apparent in O'3-layered $Na_3Ni_2SbO_6$ cathode material. This strategy is successful in obtaining a sloping voltage curve without distinct plateaus—an indication of suppression of the underlying structural phenomena that cause them—at doping concentrations of $x \geqslant 0.3$. The first-cycle coulombic efficiency of the doped compounds is much greater than the starting compound, presumably owing to a kinetic barrier to reforming the full O'3-layered starting materials within the voltage range of 2.5–4.3 V vs Na^+/Na. Sodium doping into the MO_2 layer thus remains a promising strategy for enabling commercial Na_xMO_2 cathodes, but further development is required to lower the kinetic barrier for sodium reinsertion into these materials in a useful voltage range to maximize their reversible capacity.
 [DOI: 10.1149/1945-7111/ac60eb]

Manuscript received February 2, 2022. Published April 4, 2022. *This paper is part of the JES Focus Issue on Focus Issue In Honor of John Goodenough: A Centenarian Milestone.*

Supplementary material for this article is available online

Sodium batteries have emerged as a promising alternative to present Li-ion batteries due to the abundance and low-cost of sodium. However, the technical metrics of secondary sodium batteries still pale in comparison to their lithium counterparts. Layered Na_xMO_2 oxides have been under investigation for enabling a commercial Na-ion battery for decades owing to their high specific capacities stemming from limited additional species in the structure aside from sodium and fast Na^+ diffusion in the interlayer space during cycling.[1,2] However, intrinsic structural nuances that occur during cycling—sodium ordering and layered-layered phase transitions—cause numerous plateaus in their voltage curve.[3] This phenomenon, often termed as an "Electrochemical Devil's Staircase," hinders the practicality of layered sodium oxides as cathode materials in commercial batteries.[4]

O'3-layered $Na_3Ni_2SbO_6$ ($Na[Ni_{2/3}Sb_{1/3}]O_2$) has been evaluated as a cathode material for sodium-ion batteries and has shown good specific capacity and rate capability if sufficient levels of carbon in the cathode composite are used.[5] This material experiences two layered-layered structural transitions during cycling between 2.5 to 4 V vs Na^+/Na, resulting in numerous plateaus in its voltage curve.[6–8] Previous work on sodium substitution for transition-metals in the MO_2 layer of Na_xMO_2 materials showed promise for suppressing the structural issues of these materials during cycling, such as Na^+ substitution for Ni^{2+} in the honeycomb ordered O'3-layered $Na_3Ni_{1.5}TeO_6$—or $Na_{5/6}[Na_{1/6}Ni_{1/2}Te_{1/3}]O_2$ written in the classical layered notation.[9] However, for the layered nickel-tellurate system, the chemical formula is such that this substitution can take place with charge compensation coming from vacancies formed in the structure. The structurally analogous honeycomb ordered O'3-layered $Na_3Ni_2SbO_6$ provides a prime candidate to further tailor the material composition through sodium doping into the MO_2 layer to reap the benefits of its specific capacity and good rate capability while ridding the voltage curve of the voltage plateaus attributed to the layered-layered structural transitions experienced during cycling.

For the fully occupied lattice of the O'3-layered $Na_3Ni_2SbO_6$ material, a counter dopant is needed to charge compensate the substitution of single valent Na^+ for the divalent Ni^{2+}. Fe^{3+} was chosen as it has a similar size to Ni^{2+} and can be easily synthesized and doped into the layered structure for sodium as demonstrated by O3-layered $NaFeO_2$.[10–12] The final composition of the series of materials synthesized and studied in this work is $Na_{3+x}Ni_{2-2x}Fe_xSbO_6$ ($0 \leqslant x \leqslant 0.5$). This strategy was successful in mitigating the negative effects on electrochemical performance of the materials by sodium ordering and MO_2 layer gliding during cycling. However, the reversibility of the intercalation/deintercalation process during their first charge/discharge cycle became quite poor even at low concentrations of Fe^{3+} in the doped materials. The results and observations gleaned from this study can be used to further the development of layered Na_xMO_2 oxides towards practical applications.

Experimental

Materials and synthesis.—Materials of the $Na_{3+x}Ni_{2-2x}Fe_xSbO_6$ ($0 \leqslant x \leqslant 0.5$) formula were prepared with a traditional solid-state synthesis. The precursor materials for synthesis were Na_2CO_3 (99.8%, Acros Organics), NiO (99%, Alfa Aesar), Fe_2O_3 (99.9%, GFS Chemicals), and Sb_2O_3 (99%, Aldrich). Stoichiometric amounts of each precursor were ground in a mortar and pestle and pressed into pellets before being sintered at 900 °C for 24 h with an intermittent grinding and pelletization step after the first 12 h to ensure homogeneity within the samples. The materials were then ground and pelletized a final time before sintering at 1000 °C for 12 h to obtain the final O'3- $Na_{3+x}Ni_{2-2x}Fe_xSbO_6$ materials. All sintering steps were performed in air with a heating and cooling rate of 10 °C min^{-1}.

X-ray diffraction.—A Rigaku Miniflex 600 (Cu Kα radiation) was used to perform all X-ray diffraction measurements. Each diffraction pattern was obtained in continuous mode from 10° to 80° 2θ. Diffraction patterns of the as-prepared materials were performed with a scan rate of 2° min^{-1} while spinning the sample to include as many crystallite orientations as possible within the diffraction

[z]E-mail: hadi.khani@austin.utexas.edu; nicholas.grundish@utexas.edu

geometry of the instrument during data acquisition. Ex situ X-ray diffraction of electrodes as-prepared, cycled to full charge, and after one full charge/discharge cycle were performed in continuous scanning mode from 10° to 80° 2θ at a scan rate of 1° min^{-1} in an air-sensitive sample holder loaded in an Ar-filled glove box (MBraun, $O_2 < 0.1$ ppm, $H_2O < 0.1$ ppm). Le Bail refinements were performed with the FullProf software to verify the phase purity of each material and obtain the lattice parameters of each unit cell for comparison. The Vesta 3D structure visualization program was used to develop all structural images used in this work.[13]

Solid-state nuclear magnetic resonance spectroscopy.—^{23}Na solid-state nuclear magnetic resonance (NMR) spectra were acquired on a 400 MHz (9.4 T) Bruker Avance III HD spectrometer with a Bruker 4 mm HXY probe at a magic angle spinning (MAS) frequency of 13 kHz. To improve the resolution of the spectra and obtain isotropic resonances in the absence of spinning sidebands, the pj-MATPASS sequence was used with 32 slices in the F2 dimension and 640 scans per slice.[14] For each system, the 2D pj-MATPASS spectra were sheared in the F2 dimension and subsequently summed in the F1 dimension to give a resulting 1D NMR spectrum that approximates the infinite spinning limit, as shown in previous studies.[9] Spectra were acquired with a $\pi/2$ pulse length of 2.2 μs optimized on solid NaCl at a power of 80 W. NaCl was used as a secondary shift reference at 7.21 ppm (relative to 1 M NaCl(aq)). All NMR measurements in this work were obtained with a short recycle delay of 0.01 s to maximize the signal from paramagnetic environments with short relaxation delays. The 1D summed ^{23}Na pj-MATPASS spectrum for the $Na_{3.2}Ni_{1.6}Fe_{0.2}SbO_6$ sample was deconvoluted using the DMFIT software package.[15] Combined 50:50 Gaussian/Lorentzian peaks were used to fit all environments, and in the final stage of the fitting procedure, the peaks positions, widths, and intensities of all environments were allowed to refine.

Density functional theory calculations.—Structural and NMR properties for pristine $Na_3Ni_2SbO_6$ and Na-Fe substituted $Na_3Ni_2SbO_6$ structures were calculated with first principles calculations. All energies and NMR properties in this work were calculated with density functional theory (DFT) by using the projector augmented wave (PAW) approach in the VASP code.[16,17] The Perdew−Burke−Ernzerhof (PBE) functional was used for all calculations and a Hubbard U correction (DFT + U) was applied to Ni and Fe 3d states to correct for errors associated with electron localization in strongly correlated systems.[18,19] The rotationally invariant version of DFT + U proposed by Dudarev et al. was used with U_{eff} values of 6.2 and 5.3 eV for Ni and Fe, respectively, consistent with previous work.[20,21] In the PAW pseudopotentials used, p states were treated as valence states for Na, Ni and Fe (_pv) and the standard pseudopotentials were used for Sb and O. All calculations performed in this work were spin polarized.

The unit-cell parameters and atomic positions of $Na_3Ni_2SbO_6$ ($C2/m$) and Na_4FeSbO_6 ($P3_112$) unit cells were fully optimized in the ferromagnetic state until the force on any atom was smaller than 0.01 eV Å, with an energy convergence criterion of 1×10^{-6} eV.[12] The Brillouin zone was sampled with a Γ-centered k-point mesh (mesh density ⩾ 20 Å) and a planewave cutoff of 520 eV. For NMR calculations, a $2 \times 1 \times 2$ supercell was created of the $Na_3Ni_2SbO_6$ unit cell. The energy and NMR properties of Na–Fe substitutions were also tested with the $2 \times 1 \times 2$ supercell in which Na and Fe atoms were substituted for Ni atoms within the structure, and the position of all atoms were allowed to relax under fixed cell conditions. The formation energy of the Na–Fe substituted cell ($Na_{3+x}Ni_{2-2x}Fe_xSbO_6$) was calculated as:

$$\Delta E = E(Na_{3+x}Ni_{2-2x}Fe_xSbO_6) - (1 - x)E(Na_3Ni_2SbO_6) - xE(Na_4FeSbO_6) \quad [1]$$

Where $E(Na_3Ni_2SbO_6)$ and $E(Na_4FeSbO_6)$ are the energies of the fully optimized $Na_3Ni_2SbO_6$ and Na_4FeSbO_6 unit cells, respectively. Two configurations were considered for the Na–Fe substituted cell in which the Na and Fe atoms were introduced as 1st nearest neighbors, and additionally, separated by ~6.2 Å within the transition-metal layer.

The Fermi contact shifts on the ^{23}Na nuclei were calculated with nominally 0 K DFT calculations as described in previous studies.[22,23] The Fermi contact shifts associated with individual M–O–Na (M=Ni or Fe) bond pathway contributions were calculated using the spin flipping approach from a previous study by Middlemiss and coworkers.[23] The Fermi contact contributions calculated at 0 K were scaled to the finite temperature paramagnetic regime of the NMR measurements with a scaling factor, Φ, defined as:

$$\Phi = \frac{B_0 \mu_{eff}^2}{3k_B g_e \mu_B S_{form}(T - \theta)}$$

where B_0 is the external magnetic field (9.4 T), k_B is Boltzmann's constant, S_{form} is the formal spin angular momentum quantum number of Ni^{2+} ($S_{form} = 1$) or Fe^{3+} ($S_{form} = 5/2$), g_e is the free electron g factor (equal to 2.0023), μ_B is the Bohr magneton, T is the experimental temperature, μ_{eff} is the effective magnetic moment, and θ is the Weiss constant. The value of T at 13 kHz MAS was taken as 320 K to account for frictional heating. Spin only values of $\mu_{eff} = 2.83$ and 5.92 μ_B were used for pathways involving Ni^{2+} and Fe^{3+}, respectively. A small, positive Weiss constant of $\theta = 12$ K was assumed for all calculations from previous experimental measurements of the magnetic structure in $Na_3Ni_2SbO_6$.[24] The scaling factors for Ni^{2+} and Fe^{3+} pathways were 1.37×10^{-2} and 2.39×10^{-2}, respectively.

Electrode preparation.—Active material and TIMCAL Super P carbon black (MTI Corp.) were ground together in a mortar and pestle before being added to a solution of 5 wt% polyvinylidene fluoride (PVDF) in N-methyl-2-pyrrolidone (NMP) such that the final composition of the electrode was 70 wt% active material, 20 wt% Super P carbon black, and 10 wt% PVDF. Additional NMP was added as needed until the viscosity of the mixture was appropriate for casting. The electrode slurry was stirred overnight with a magnetic stir bar before being doctor bladed onto a carbon-coated aluminum foil current collector (MTI Corp.). The NMP in the cast electrode sheet was allowed to evaporate in a fume hood before being dried in a vacuum oven overnight at 100°C. Finally, composite electrode discs (12 mm in diameter) were punched and immediately transferred into the glove box for cell assembly and electrochemical characterization of the O'3-$Na_{3+x}Ni_{2-2x}Fe_xSbO_6$ active materials.

Cell assembly and electrochemical testing.—2032-coin cells were prepared in an Ar-filled glove box for electrochemical characterization of the O'3- $Na_{3+x}Ni_{2-2x}Fe_xSbO_6$ active materials. The cells were assembled with a sodium-metal anode, 1 M $NaClO_4$ (99%, Alfa Aesar) in 90% propylene carbonate (99%, Aldrich) with 10% fluoroethylene carbonate (>99%, Aldrich) as the electrolyte (PC:FEC, 9:1, v/v), and a Whatman glass fiber separator. The same electrochemical cell format was used for all electrochemical tests performed in this work. The assembled coin cells were cycled galvanostatically with a Neware battery cycling unit in the voltage range of 2.5–4.3 V vs Na^+/Na at a C-rate of C/20. The C-rate of each material was calculated assuming two sodium-ions per formula unit could be reversibly intercalated from the material. This assumption was developed from the results observed from the initial report of the electrochemical performance of the $Na_3Ni_2SbO_6$ material.[5] Two-electrode cyclic voltammetry (CV) and electrochemical impedance spectroscopy (EIS) were performed on the assembled coin cells with a Bio-Logic VMP-300 potentiostat. The CVs were collected on cells with the $Na_{3+x}Ni_{2-2x}Fe_xSbO_6$ materials as the working electrode and sodium metal serving as the counter and reference electrode. The cells were scanned at a rate of 0.05 mV s^{-1} to an upper vertex potential of 4.5 V vs Na^+/Na and a lower vertex potential of 2.5 V vs Na^+/Na. EIS was performed on as-prepared cells in the frequency range of 200 kHz to 100 mHz with a 10 mV perturbation voltage.

Samples for ex situ X-ray diffraction were prepared by disassembling coin cells at various states of charge after cycling at a C/20 rate to the terminal voltage. Prior to data collection, the cycled electrodes for X-ray diffraction were washed with PC to remove any excess $NaClO_4$ salt from the sample. The electrodes were then allowed to dry overnight in the glovebox before being transferred to the diffractometer with an air-sensitive sample holder.

Results and Discussion

Materials synthesis and structure.—The $Na_{3+x}Ni_{2-2x}Fe_xSbO_6$ ($0 \leqslant x \leqslant 0.5$) series of materials were synthesized with a traditional solid-state reaction in air with carbonate and oxide precursor materials. These materials crystallize in the *C2/m* space group and were verified to be pure phase with powder X-ray diffraction (Fig. 1a). Figure 1b depicts a model of the structure of these materials developed through observation of the parent $Na_3Ni_2SbO_6$ material. These materials adopt a layered structure with alternating sodium and $[Na_{x/3}Ni_{2/3-2/3x}Fe_{x/3}Sb_{1/3}]O_2$ layers when the full formula of the material is reduced to the traditional $NaMO_2$ layered formula. Sodium sits in octahedral sites in the interlayer space while the MO_6 octahedra in the MO_2 layer are honeycomb ordered with every SbO_6 octahedra being surrounded by six $[Na,Ni,Fe]O_6$ octahedra. This honeycomb ordering provokes a monoclinic distortion to the unit cell relative to the traditional hexagonal unit cell of classical layered AMO_2 (A = Li or Na) compounds where all *M*-ions are of a single element. These structural features give the $Na_{3+x}Ni_{2-2x}Fe_xSbO_6$ ($0 \leqslant x \leqslant 0.5$) materials an O'3-layered structure according to the notation set forth by Delmas et al. for layered compounds.[25]

The O'3-$Na_3Ni_2SbO_6$ compound has been studied previously and noted for the presence of faults in its layer stacking depending on the heating procedure used during synthesis.[8] The method used in this work for the synthesis of the $Na_{3+x}Ni_{2-2x}Fe_xSbO_6$ ($0 \leqslant x \leqslant 0.5$) series is comparable to the route that induces stacking faults in the starting undoped material.[5] These stacking faults are evidenced by the diffuse diffraction peaks shown in the superstructure region of the diffraction patterns in Fig. 1 between 18.5°–24° 2θ and made a full Rietveld refinement of the diffractograms with a satisfactory fit difficult. Therefore, Le Bail refinements (Supporting Information, Figures S1-S6 (available online at stacks.iop.org/JES/169/040504/mmedia)) were performed with the superstructure region excluded from the refinement to obtain the lattice parameters of each material, which are summarized in Table I. Solid-state ^{23}Na NMR was performed to delineate the individual sodium environments in more detail as further discussed below.

The unit-cell parameters of the $Na_{3+x}Ni_{2-2x}Fe_xSbO_6$ ($0 \leqslant x \leqslant 0.5$) materials noticeably changed with the addition of Na^+ and Fe^{3+} for Ni^{2+}. The value of csinβ is indicative of the MO_2 interlayer distance; the increase of this value with increasing value of x in the material formula indicates that the doping was successful with the Na^+ and Fe^{3+} co-doping the Ni^{2+} sites in the MO_2 layer. Although doping Na^+ in the MO_2 layer was previously only observed in 4d transition-metal compounds, such as Na_2RuO_3 (or $Na[Na_{1/3}Ru_{2/3}]O_2$), recent reports have demonstrated this phenomenon in honeycomb ordered nickel-tellurate compounds.[9,26,27] Thus, the honeycomb ordering of the $Na_{3+x}Ni_{2-2x}Fe_xSbO_6$ ($0 \leqslant x \leqslant 0.5$) materials allows for the possibility that sodium is residing in the MO_2 layer of the materials. A more localized structural characterization was required to confirm this hypothesis formed from the indirect evidence garnered from the Le Bail refinements of the X-ray diffraction data.

The local Na^+ environments within the structure of the $Na_{3+x}Ni_{2-2x}Fe_xSbO_6$ ($0 \leqslant x \leqslant 0.5$) materials were investigated with a combination of DFT calculations and solid-state ^{23}Na NMR. A $2 \times 1 \times 2$ supercell ($Na_{24}Ni_{16}Sb_8O_{48}$) of the *C2/m* $Na_3Ni_2SbO_6$ unit cell was created and two 1st nearest neighbor (nn) Ni sites were substituted for Na and Fe (Fig. 2). A low formation energy of 62 meV per formula unit was calculated for the Na–Fe substituted supercell ($x = 0.125$) from Eq. 1, supporting the possibility of Na/Fe introduction into the Ni layer, particularly at high-temperature during synthesis. The interaction energy of Na and Fe substitution was calculated by modelling a configuration in which the Na and Fe dopants were separated by $\sim$ 6.2 Å within the Ni layer. The "separated" configuration was 43 meV higher in energy than the 1st nn configuration, indicating a weak preference for Na–Fe binding within the Ni layer.

The pristine $Na_3Ni_2SbO_6$ and Na–Fe doped supercell configurations were then used to calculate the ^{23}Na NMR properties of the different Na sites. The Ni and Fe sites within the supercell structures had magnetic moments of 1.8 μ_B for Ni^{2+} (S = 1, $t_{2g}^6e_g^{*2}$) and 4.3 μ_B for high spin Fe^{3+} (S = 5/2, $t_{2g}^3e_g^{*2}$). The dominant contribution to the ^{23}Na NMR spectrum in paramagnetic materials is due to the Fermi contact interaction where the unpaired spin density on the transition metals is transferred to the Na nuclear position via an intermediate oxygen ligand. As discussed in previous studies, the total ^{23}Na shift can be decomposed into individual *M*–O–Na (*M* = Ni^{2+} or Fe^{3+}) bond pathway contributions.[8,9,28,29] In the $Na_{3+x}Ni_{2-2x}Fe_xSbO_6$ ($0 \leqslant x \leqslant 0.5$) structure, there are three Na sites (Fig. 3): Na(1) and Na(2) within the Na layer and Na(3) sites in the transition-metal layer. Na(1) and Na(2) sites experience both

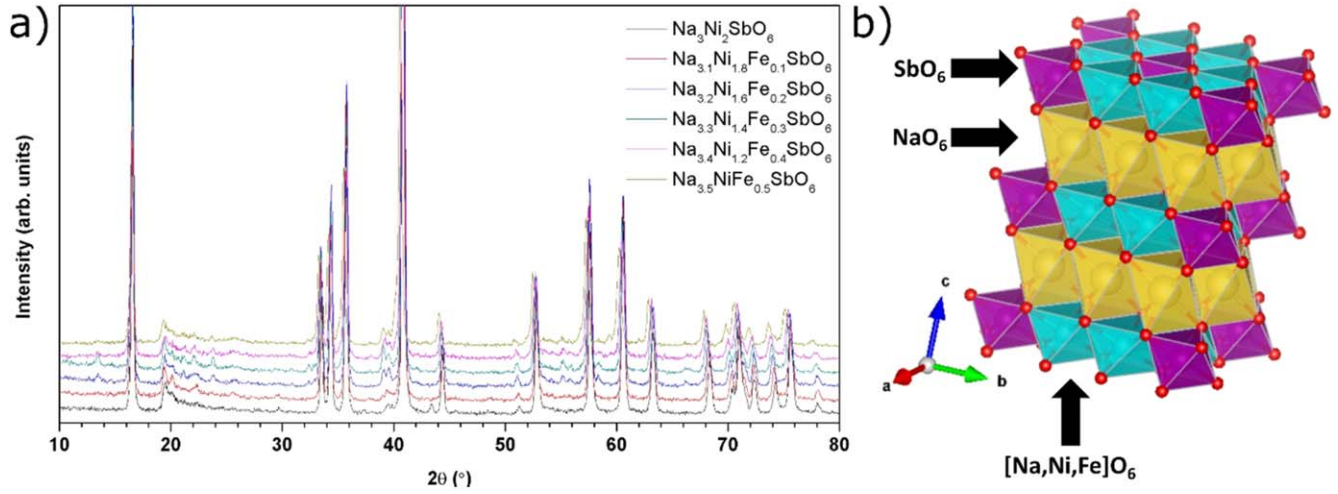

Figure 1. (a) Powder X-ray diffraction patterns of the $Na_{3+x}Ni_{2-2x}Fe_xSbO_6$ ($0 \leqslant x \leqslant 0.5$) series of materials. Le Bail refinements were performed on all powder diffraction patterns to obtain lattice parameters for each material and confirm phase purity (Support Information, Figs. S1–S6). (b) Depiction of the O'3-layered $Na_{3+x}Ni_{2-2x}Fe_xSbO_6$ ($0 \leqslant x \leqslant 0.5$) honeycomb ordered structure.

Table I. Lattice parameters obtained from Le Bail refinements for $Na_{3+x}Ni_{2-2x}Fe_xSbO_6$ materials indexed to the *C2/m* space group.

	x in $Na_{3+x}Ni_{2-2x}Fe_xSbO_6$					
	0	0.1	0.2	0.3	0.4	0.5
a (Å)	5.291	5.291	5.291	5.301	5.310	5.321
b (Å)	9.170	9.172	9.154	9.164	9.160	9.225
c (Å)	5.620	5.641	5.641	5.647	5.656	5.676
β (°)	108.194	108.303	108.165	108.198	108.183	108.287
csinβ (Å)	5.339	5.356	5.360	5.365	5.374	5.389
R_{wp}	17.8	16.4	19.4	21.1	18.2	16.9
R_{Bragg}	3.64	4.00	4.89	5.51	2.95	2.27
χ^2	5.52	6.37	6.48	7.10	5.02	3.95

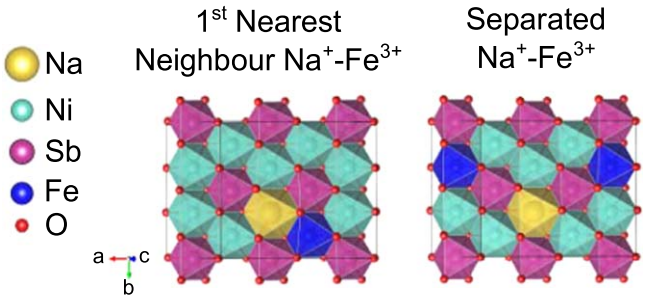

Figure 2. Schematic representation of Na–Fe doped $Na_3Ni_2SbO_6$ supercells with Na–Fe substitution in the 1st nearest neighbour configuration vs separated by ~6.2 Å.

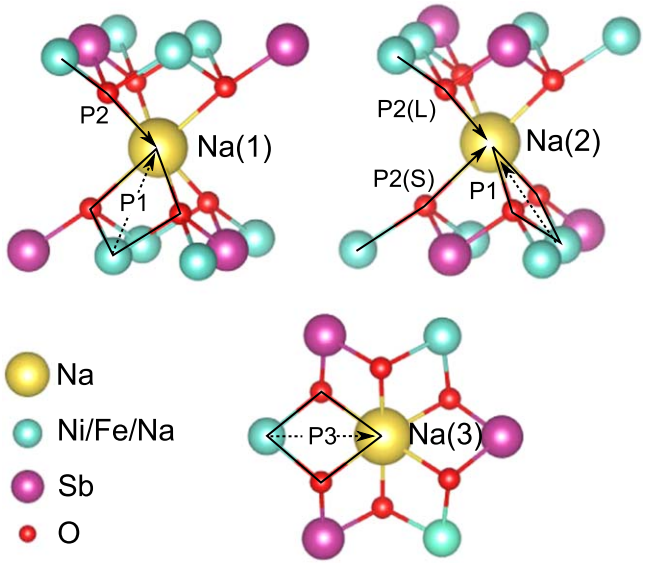

Figure 3. Schematic diagram of *M*–O–Na (*M* = Ni, Fe or Na(3)) bond pathways around the three Na sites within the $Na_{3+x}Ni_{2-2x}Fe_xSbO_6$ structure: Na(1), Na(2), and Na(3). Spin transfer along 90° (P1) and 180° (P2) *M*–O–Na pathways for Na(1) and Na(2) sites and 90° (P3) *M*–O–Na pathways for Na(3) sites are indicated with black lines. (P2) pathways for Na (2) sites are broken down into short (S) and long (L) contributions based on the *M*–O–Na bond distances.

90° (P1) and 180° (P2) *M*–O–Na pathways with Ni or Fe sites in the transition-metal layer. Na3 sites in the transition metal layer only experience 90° (P1) *M*–O–Na pathways with neighboring Ni or Fe sites within the same transition-metal layer. The size of the Fermi contact for each type of pathway contribution was calculated from first principles and is shown in Table II.

As seen in Table II, the 90° Ni^{2+}-O-Na P1 pathway results in a small negative shift (~ −50 ppm) for both the Na(1) and Na(2) sites, but the 90° Fe^{3+}-O-Na P1 peak leads to a small positive shift. The negative shift for 90° Ni^{2+} results from a weak "polarization"-type mechanism involving the half-occupied Ni e_g* orbital, two orthogonal O2p orbitals, and the Na 2 s orbital, as discussed in previous studies.[28] The positive shift for 90° Fe^{3+} results from a delocalization-type mechanism in which the half-occupied Fe t_{2g} orbital overlaps with a single O2p orbital and the Na 2 s orbital.

The 180° *M*–O–Na P2 pathways for both Ni^{2+} and Fe^{3+} are both large and positive, due to a delocalization-type mechanism involving a half-occupied e_g* orbital, an O2p orbital, and the Na 2 s orbital. For both the Na(1) and Na(2) sites, the P2 pathways for Fe^{3+} are around a factor of 2 larger than the P2 pathways for Ni^{2+}, due to the larger spin of Fe^{3+} (S = 5/2) compared to Ni^{2+} (S = 1) which leads to a larger local scaling factor. The Na(1) site contains four Ni–O–Na P2 pathways in the $Na_3Ni_2SbO_6$ structure with equivalent bond lengths (4.48 Å). The Na(2) site contains two short P2 pathways (4.48 Å) and two long P2 pathways (4.53 Å), which will subsequently be referred to as P2(S) and P2(L), respectively. The longer P2(L) pathway results in a lower shift than the P2(S) pathway for both Ni and Fe, due to the smaller amount of spin density transfer over longer bond lengths.

The Na(3) sites within the transition-metal layer only contain 90° *M*–O–Na P3 pathways, which are analogous to P1 pathways. However, the shorter *M*-Na distances of P3 pathways (~3.1 Å) leads to a larger shift compared to longer P1 (~3.2 Å) pathways.

The local Na environments in the solid-state ^{23}Na NMR spectra of the $Na_{3+x}Ni_{2-2x}Fe_xSbO_6$ ($0 \leqslant x \leqslant 0.5$) series can be rationalized with these calculated shift contributions. Solid-state ^{23}Na NMR spectra were acquired for each as-prepared material as shown in Fig. 4a. The base $Na_3Ni_2SbO_6$ structure contains two resonances at 1542 and 1392 ppm, which can be assigned to the Na(1) and Na(2) sites, respectively, and is consistent with previous NMR studies.[6,8] The shifts of these two sites are also in excellent agreement with the computationally predicted shifts in Table II for each site of 1475 and 1374 ppm, respectively. Both the Na(1) and Na(2) sites contain the same number of P1 pathways, which have very similar shift contributions. The main shift difference between the sites results from the longer P2(L) pathways in the Na(2) site, which results in a smaller shift contribution of around 50 ppm per pathway.

For the $Na_{3+x}Ni_{2-2x}Fe_xSbO_6$ samples with $x > 0$, the spectra in Fig. 4a show additional shoulders that grow on either side of the original peaks with additional peaks present at smaller positive and negative frequencies, indicating that Na^+ and Fe^{3+} are being introduced into the MO_2 layer of the structure. For all spectra, the maximum intensity has been scaled to one to allow for the variation in the local environments to be compared. An absolute quantitative comparison of the spectral intensities is not possible as the spectra have not been weighted to account for differences in relaxation time of different environments or sample mass. The spectrum of $Na_{3.2}Ni_{1.6}Fe_{0.2}SbO_6$ was deconvoluted as shown in Fig. 4b. A

Table II. Fermi contact *M*–O–Na (*M*=Ni^{2+} or Fe^{3+}) bond pathway contributions for the pristine and Na–Fe substituted $Na_{3+x}Ni_{2-2x}Fe_xSbO_6$ structures calculated with DFT. The total number of P1, P2, and P3 *M*–O–Na pathways for the Na(1), Na(2), and Na(3) sites is given. All pathway contributions are scaled to 320 K.

Na Site	Pathway	*M*–O–Na Angle (°)	Total no. per site	Pathway Contribution (ppm)		Shift in Pristine $Na_3Ni_2SbO_6$ (ppm)
				Ni^{2+}–O–Na	Fe^{3+}–O–Na	
Na(1)	P1	90	4	−50	74	1475
	P2	180	4	419	915	
Na(2)	P1	90	4	−49	16	1374
	P2(S)	180	2	419	856	
	P2(L)	180	2	366	685	
Na(3)	P3	90	3	−78	474	—

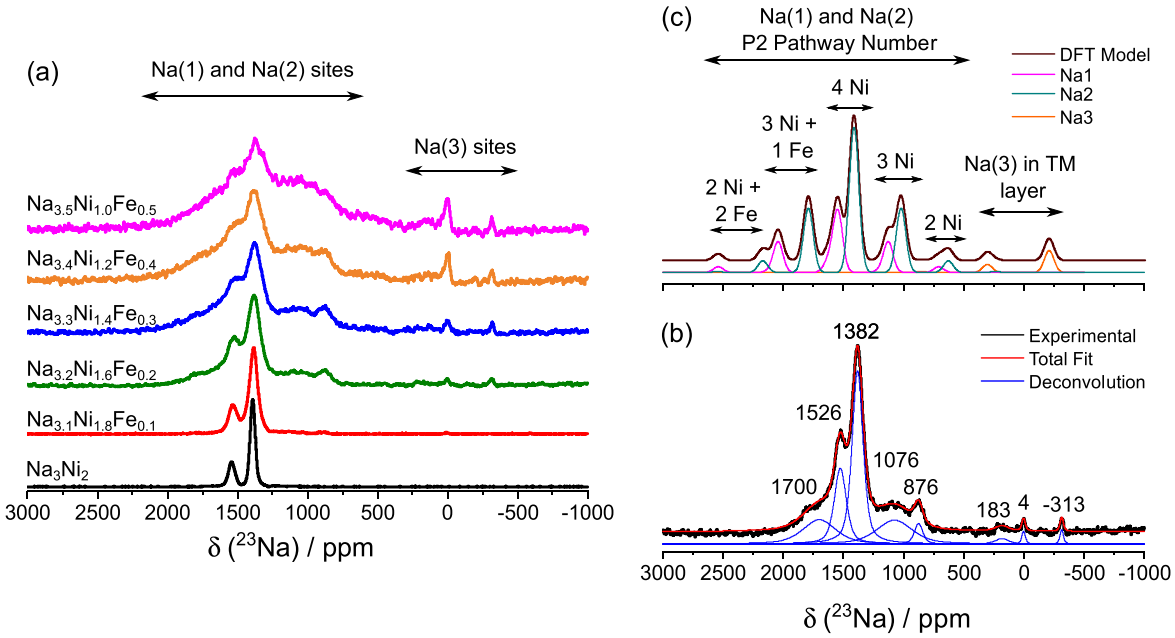

Figure 4. (a) ^{23}Na NMR spectra of $Na_{3+x}Ni_{2-2x}Fe_xSbO_6$ samples at 9.4 T and 13 kHz MAS. 1D spectra are produced from summation of 2D pj-MATPASS spectra, with the maximum intensity of each spectrum scaled to one for comparison. (b) Deconvolution of $Na_{3.2}Ni_{1.6}Fe_{0.2}SbO_6$ spectrum showing the total fit (red) and individually deconvoluted peaks (blue). (c) Random solution model of possible ^{23}Na environments in $Na_{3.2}Ni_{1.6}Fe_{0.2}SbO_6$ with Ni^{2+}–O–Na and Fe^{3+}–O–Na bond pathway contributions in Table II calculated with DFT. The number of P2 pathways to either Ni^{2+} or Fe^{3+} for Na(1) and Na(2) environments is indicated, along resonances associated with Na(3) sites in the transition metal layer.

good fit could be obtained with 8 peaks located at 1700, 1526, 1382, 1076, 876, 183, 4, and −313 ppm. Although ^{23}Na is a quadrupole nucleus with nuclear spin of I = 3/2, minimal distortion of the peak line shapes was observed due to quadrupole effects. This lack of observed distortion is due to the combination of the moderately high magnetic field (9.4 T) used in this study and the relatively small quadrupole coupling constant, $C_Q \sim 3$ MHz for Na(1) and Na(2) sites in $Na_3Ni_2SbO_6$ as reported in previous studies.[8]

A random solution model (Fig. 4c) analogous to previous studies was used to help assign the environments in Figs. 4a and 4b with the bond pathway contributions in table 2. The $Na_{3.2}Ni_{1.6}Fe_{0.2}SbO_6$ (x = 0.2) composition was again used as a model system.[30,31] The total number of possible *M*–O–Na (*M* = Ni^{2+}, Fe^{3+} or Na3) pathway contributions were calculated for each Na site along with their corresponding probabilities at the x = 0.2 composition. Na3–O–Na pathways were assumed to result in a zero shift contribution. For Na (2) sites, an average of the P2(S) and P2(L) values was used when considering the contribution from P2 pathways. As the shift contribution of P2 pathways for Na(1) and Na(2) sites is considerably larger than P1 pathways, an additional simplification was made in which the shifts and intensities of Na sites with the same types of P2 pathways but different types of P1 pathways were combined using a weighted average. A Gaussian peak with a width of 10 ppm was then added to each environment to allow for comparison with experimental spectra, with the result shown in Fig. 4c.

From comparison of Figs. 4b and 4c, the agreement between the peak positions in the experimental and computationally derived models suggest that the random solution model in the former case provides a good approximation of the true distribution of Ni, Fe, and Na sites in the transition metal layer. The most intense peaks in the spectrum of Fig. 4c between 1300–1600 ppm correspond to Na(1) and Na(2) sites with four 180° Ni^{2+}–O–Na P2 pathways and no 180° Fe^{2+}–O–Na P2 pathways, analogous to the Na(1) and Na(2) sites in the pristine $Na_3Ni_2SbO_6$. This observation is expected due to the relatively low fraction of Fe substitution in the $Na_{3.2}Ni_{1.6}Fe_{0.2}SbO_6$ system. The shoulder at 1700 ppm in Fig. 4c can be assigned to Na (1) and Na(2) sites with one Fe^{3+}–O–Na P2 pathway. The shoulders at lower ppm from 800–1100 ppm can be assigned to Na(1) and Na (2) sites with three 180° Ni^{2+}–O–Na P2 pathways with one Na3–O–Na P2 pathway that contributes zero Fermi contact shift. The peaks at 876 and 1076 ppm with one Na3 P2 pathway have a similar intensity to the broad peak at 1700 ppm with one Fe^{3+} P2 pathway in Fig. 4b, which is consistent with the expected one to one ratio of Na3 to Fe sites in the $Na_{3.2}Ni_{1.6}Fe_{0.2}SbO_6$ structure.

From Fig. 4c, the Na(3) site in the transition metal layer, which only contains 3 P3 pathways, is expected to have a negative shift of −209 ppm for three Ni^{2+} neighbors and a positive shift of 304 ppm for 2 Ni^{2+} and 1 Fe^{3+} neighbors. These computed shifts are consistent with the experimentally observed resonances of −313 and 183 ppm, respectively, further highlighting that Na has been introduced into the transition-metal layer. The shift at 4 ppm is likely due to diamagnetic impurities such as carbonates, but there may be a small contribution from Na(3) sites with only Na(3) neighbors, analogous to ^{23}Na local environments in the Na_3SbO_4 *P2/c* structure.

As the fraction of Na and Fe increases in the $Na_{3+x}Ni_{2-2x}Fe_xSbO_6$ structure, it can be seen that the peaks associated with the Na(1) and Na(2) sites in the pristine $Na_3Ni_2SbO_6$ structure progressively decrease at the expense of Na(1) and Na(2) type environments with Fe^{3+} or Na(3) neighbors, leading to a broad distribution of shifts from 700–2000 ppm at the most highly substituted sample of $Na_{3.5}NiFe_{0.5}SbO_6$—as observed in Fig. 4a. The Na(3) peaks at ∼−300 ppm and ∼180 ppm also progressively increase in intensity, highlighting that Na can be substituted into the transition-metal layer beyond the dilute limit in this family of materials.

With a firm understanding of the structural and sodium ordering in these materials, electrochemical characterization was performed to evaluate whether the doping of Na^+ and Fe^{3+} for Ni^{2+} affects the structural transition and ordering during the intercalation/deintercalation process. The baseline $Na_3Ni_2SbO_6$ material is known to undergo a layer stacking transition of O3 → O3 + P3 → P3 → P3 + O1 → O1 during charge to 4 V vs Na^+/Na.[5] However, there has been previously reported evidence that sodium doping in the MO_2 layer of materials disrupts the ordering of sodium in the adjacent interlayer space and limits the number of structural transitions across the compositional range of the material experienced during cycling.[9] Controlling these two phenomena limits the number of voltage plateaus of these materials and makes their cycling curves more practical for commercial applications.

Cyclic voltammetry was performed as an initial probe of the electrochemical consequences of doping the $Na_3Ni_2SbO_6$ materials—the results of this experiment are shown in Fig. 5. In the as-prepared $Na_3Ni_2SbO_6$ and $Na_{3.1}Ni_{1.8}Fe_{0.1}SbO_6$ materials there are two distinct sharp oxidation peaks within the voltage range of 2.5 to 4.5 V vs Na^+/Na. These sharp peaks in the voltammograms represent diffusion-limited reactions that can be attributed to Na^+ diffusion in Na(1) and Na(2) sites for the well-ordered structures on the $Ni^{2+/3+}$ redox couple.[5] The voltages observed for these materials are higher than what would normally be expected for the $Ni^{2+/3+}$ redox couple and can be attributed to the inductive effect of high valent Sb^{5+} similar to what is observed in polyanion materials that raises the ionicity of the Ni–O bond creating a larger energy difference against the Fermi level of sodium metal — a similar effect has been observed in layered materials containing Te^{6+}.[32–35] The two distinct CV peaks for these two materials agree well with the results of the ^{23}Na NMR spectra, corresponding to sodium being well-ordered among the two distinct sites within the sodium layer of the structure. At higher dopant concentrations ($x > 0.1$), the CV peaks become more diffuse, indicating that sodium is more disordered between the two sites in the interlayer space of the O'3-layered structure. After the first CV cycle for each material, the materials demonstrated much lower current for each peak (Supporting Information, Figs. S7–S12), suggesting that the materials are becoming less electrochemically active during ensuing cycles. This result gives a preliminary indication that these materials may not have superior cycle life during charge/discharge cycling. However, galvanostatic cycling was performed to further study the intercalation/deintercalation reactions of these materials.

The voltage vs composition curve for each material in the $Na_{3+x}Ni_{2-2x}Fe_xSbO_6$ ($0 \leqslant x \leqslant 0.5$) series is presented in Fig. 6. Beyond the base $Na_3Ni_2SbO_6$ composition, the first-cycle coulombic efficiency of each material is below 60%, which indicates that some structural reaction could be preventing Na^+ diffusion back into the material on first discharge. Approximately the same amount of sodium was extracted from the interlayer space of each material on the first charge cycle, but only the base material reobtained a composition anywhere near the starting material after the end of first discharge (Supporting Information, Fig. S13). Although the doped materials with higher Fe^{3+} concentrations ($x = 0.4$ and 0.5) return to similar concentrations of sodium in the material compared to the base compound, the active sodium within the interlayer space is less for the doped materials and the resulting specific capacities of the doped materials falls short of the base compound (Supporting Information, Fig. S14). However, the doped compounds show higher operating voltage due to the Na^+/Ni^{2+} ratio in compositions becoming such that the charge compensation during sodium extraction cannot be fully accommodated by the $Ni^{2+/3+}$ redox couple alone, and the higher voltage $Ni^{3+/4+}$ redox couple becomes accessible. The large first-cycle capacity fade may be attributed to a kinetic barrier to the complete reformation of the O'3-layered phase of the material as this phenomenon has been observed in the structurally analogous O'3-layered $Na_3Ni_{1.5}TeO_6$.[9] The change in voltage curves over the course of the doping series is consistent with the observed cyclic voltammograms. The base $Na_3Ni_2SbO_6$ material shows the most voltage plateaus during insertion/extraction of sodium which is attributed to sodium ordering and MO_2 slab gliding that induces layered-layered structural transitions across the accessible composition range during cycling. As Na^+ and Fe^{3+} are substituted for Ni^{2+} across the series, the number of voltage plateaus gets reduced to a single reversible plateau for the $Na_{3.3}Ni_{1.4}Fe_{0.3}SbO_6$ composition. This result is expected from observations of the ^{23}Na NMR and cyclic voltammetry as the doping disrupts the sodium ordering in the as prepared material and thus causes the voltage at which sodium is inserted/extracted to become less distinct across the compositional range of cycling. In similar systems where sodium has been introduced into the MO_2 layer, such as the $Na_3Ni_{1.5}TeO_6$ system, structural transitions have been suppressed during cycling even at low concentrations of Na^+ in the interlayer space.[9] To determine whether the $Na_{3+x}Ni_{2-2x}Fe_xSbO_6$ ($0 \leqslant x \leqslant 0.5$) series experience a similar phenomenon, ex situ X-ray diffraction was performed for the $Na_{3.3}Ni_{1.4}Fe_{0.3}SbO_6$ composition. This composition was selected as it was the composition with the lowest sodium content that had a single voltage plateau during cycling.

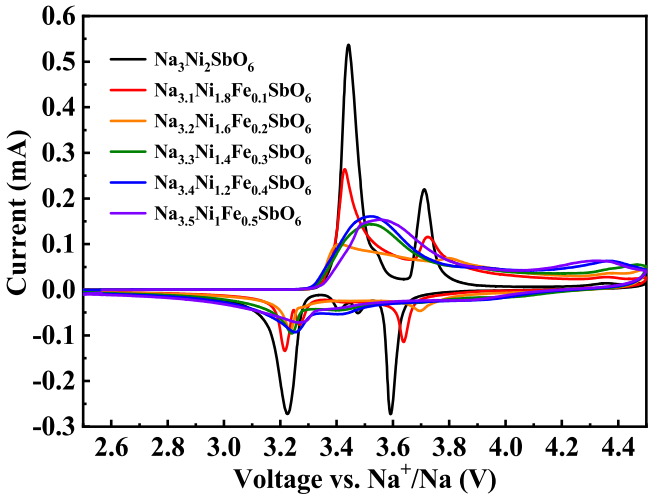

Figure 5. First cycle cyclic voltammograms of $Na_{3+x}Ni_{2-2x}Fe_xSbO_6$ ($0 \leqslant x \leqslant 0.5$) samples collected at a 0.05 mV s^{-1} scan rate against a sodium-metal anode and with 1 M $NaClO_4$ PC:FEC (9:1) (v:v) as the electrolyte.

Figure 7 presents the ex situ diffraction patterns for the $Na_{3.3}Ni_{1.4}Fe_{0.3}SbO_6$ material in a pristine electrode, charged to 4.3 V vs Na^+/Na, and after first discharge to 2.5 V vs Na^+/Na. X-ray diffraction patterns of layered materials have particular attributes that allow for the distinction between O3 and P3 layer stackings.[4,9]

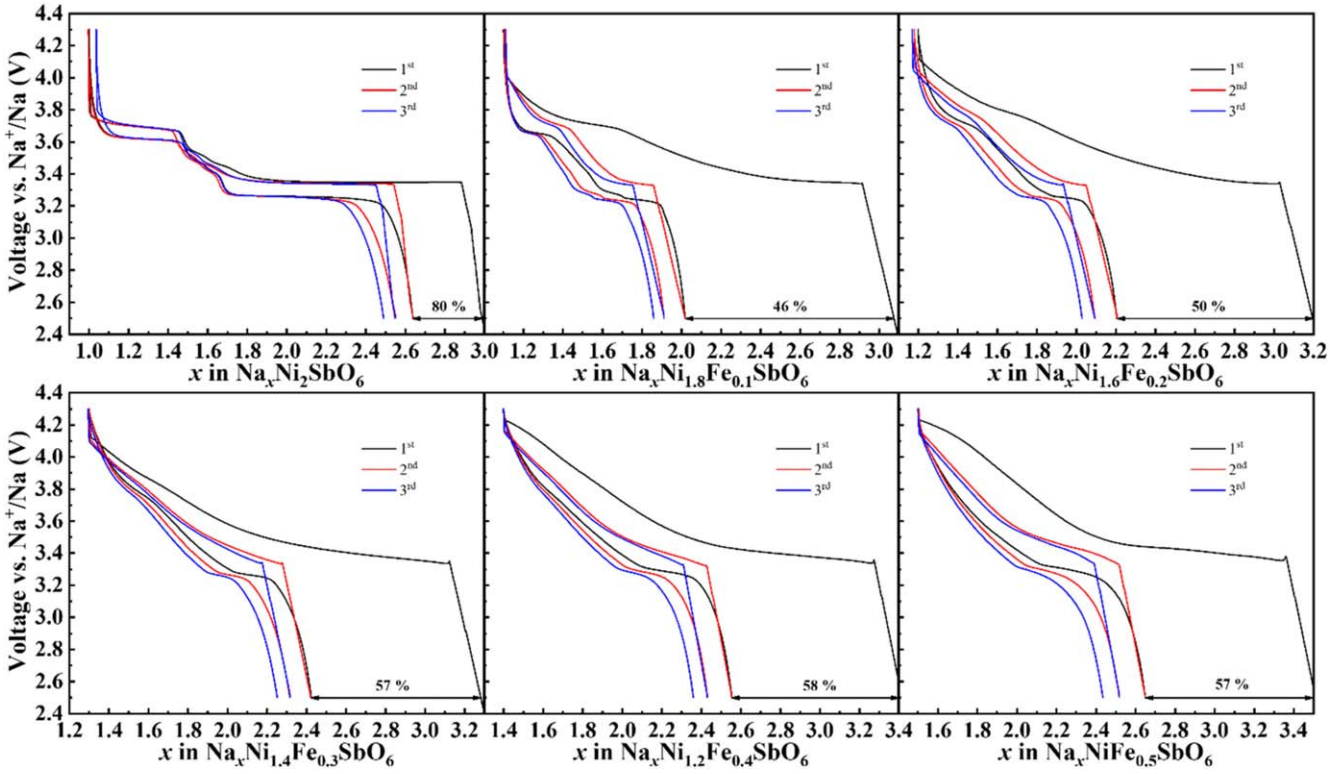

Figure 6. Voltage vs composition curves of $Na_{3+x}Ni_{2-2x}Fe_xSbO_6$ ($0 \leqslant x \leqslant 0.5$) samples galvanostatically cycled at a C/20 rate. The total sodium content within the material is shown over the first three cycles. Each cell was cycled against a sodium-metal anode with 1 M $NaClO_4$ PC:FEC (9:1) (v:v) as the electrolyte. The percentages listed in each panel represent the first-cycle coulombic efficiency for the noted material.

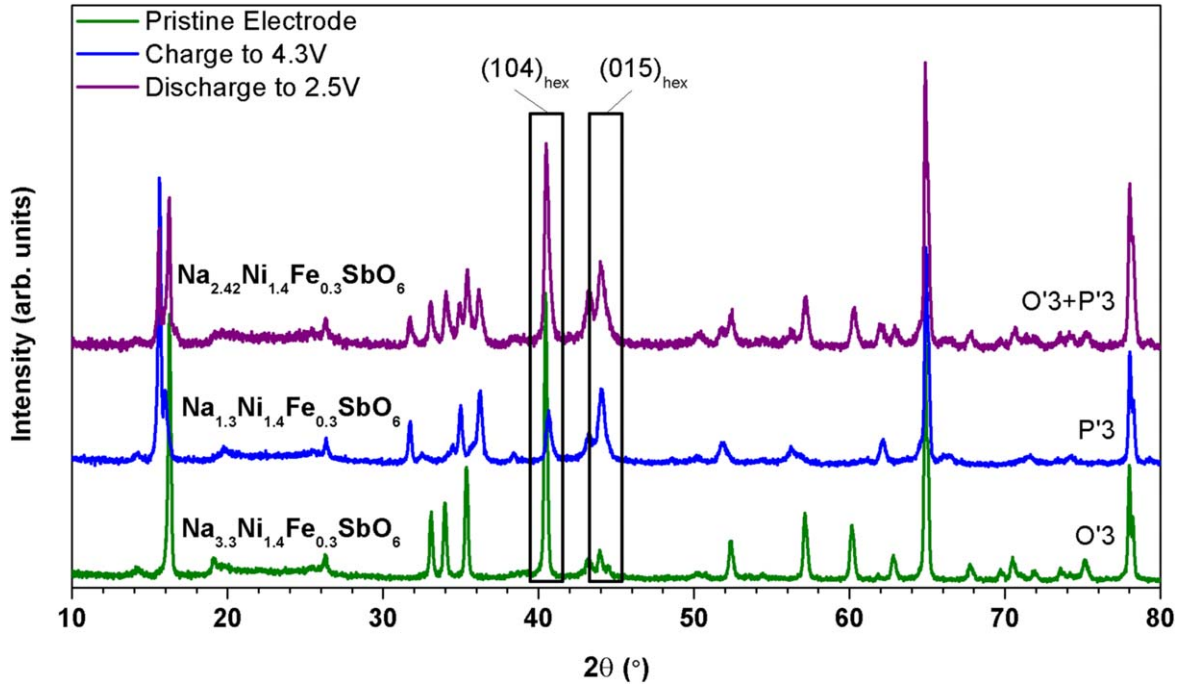

Figure 7. Comparison of the ex situ X-ray diffraction patterns for the $Na_{3.3}Ni_{1.4}Fe_{0.3}SbO_6$ material in the pristine electrode, charged to 4.3 V, and discharged to 2.5 V. The compositions of the active cathode material noted in the figure represent an average composition calculated based on the sodium that has been extracted/inserted during electrochemical cycling. The $(104)_{hex}$ and $(015)_{hex}$ peaks have been denoted with a black box to show their relative intensities and distinguish between the O3 and P3 layer stackings.

Specifically, the ratio of relative intensities of the (104) and (015) peaks when the pattern is indexed to the hexagonal unit cell is a telltale factor to distinguish whether the material has an O3 layer stacking or a P3 layer stacking. If $I_{(104)} > I_{(015)}$, then the material demonstrates O3 layer stacking. If $I_{(104)} < I_{(015)}$, then the material demonstrates P3 layer stacking. Another indication of an O3 to P3

layer stacking transition is a lowering of the (00 *l*) peak—the (003) peak for monoclinically distorted layered oxides—to a lower 2θ upon electrochemical desodiation. This lowering of the diffraction angle for the first primary diffraction peak indicates an increase in the interlayer spacing of the MO_2 layers for the material, which is consistent with the larger size of prismatic sites in P3 layered compounds compared to the octahedral sites of O3-layered compounds. The diffraction pattern of the pristine O'3-$Na_{3.3}Ni_{1.4}Fe_{0.3}SbO_6$ electrode shows a $I_{(104)}/I_{(015)}$ ratio that is greater than 1, which confirms the O3 layer stacking for the starting material. When charged to 4.3 V vs Na^+/Na, the material has a composition of $Na_{1.3}Ni_{1.4}Fe_{0.3}SbO_6$ (or $Na[Na_{0.3}Ni_{1.4}Fe_{0.3}SbO_6]$ assuming all sodium within the MO_2 layer does not migrate during cycling), and the $I_{(104)}/I_{(015)}$ ratio is less than 1, indicating that the material has transitioned to a P3 layer stacking. The diffraction pattern of the fully charged material can still be fully indexed to the *C2/m* space group, and therefore the material still demonstrates a monoclinic distortion, making the full $Na_{1.3}Ni_{1.4}Fe_{0.3}SbO_6$ material a P'3-layered compound according to Delmas notation. This result is consistent with other partially desodiated layered antimony oxides—such as the P3-layered $Na_{0.58}Cr_{0.79}Sb_{0.21}O_2$ (or $Na_{1.74}Cr_{2.37}Sb_{0.63}O_6$)—which do not have enough antimony within the MO_2 layer to induce a monoclinic distortion from honeycomb ordering, but still displays the P3 layer stacking which is expected for materials desodiated below $x < 0.7$ in Na_xMO_2 layered materials.[25,36] This observation implies that the 2:1 ratio of the *M*:(Sb/Te) ratio is important for inducing a consistent honeycomb ordering within the MO_2 layer and the resulting monoclinic distortion to the unit cell of layered antimonate or tellurate materials.

The diffraction pattern for the sample discharged to 2.5 V after charging to 4.3 V vs Na^+/Na shows the presence of two layered phases—an O'3-layered phase and a P'3-layered phase consistent with the as-prepared electrode and fully charged electrode, respectively. The presence of two phases in the fully discharged diffraction pattern is attributed to two separate factors. In the $Na_3Ni_{1.5}TeO_6$ material that had sodium substituted for Ni^{2+} in the MO_2 layer, a potentiostatic hold was needed to fully reobtain the O'3 starting phase. If a potentiostatic hold was not enforced at the end of the discharge cycle, the material remained fully in the P'3-layered phase. Thus, a kinetic barrier for sodium insertion back into the material within the cycling range down to 2.5 V vs Na^+/Na prevented the reformation of the O'3 phase. For the $Na_{3.3}Ni_{1.4}Fe_{0.3}SbO_6$ material tested here, the reformation of some O'3 phase at the end of discharge without inducing a potentiostatic hold indicates that sodium can reinsert into some parts of the material at the slow cycling rate of C/20, but not all of it. Thus, a similar effect could be taking place here of a kinetic barrier preventing the full formation of the initial O'3-layered phase after the first discharge that was partially masked by a low C/20 rate used for evaluation of the electrochemical performance of these materials that allowed for some of the material to reform the O'3-layered phase while leaving other parts of the material sodium deficient and still in the P'3-layered phase. The noted composition for the discharged material of $Na_{2.42}Ni_{1.4}Fe_{0.3}SbO_6$ can, therefore, be considered an average composition of the material, while the O'3 phase has a higher sodium composition than what is noted, and the P'3 phase has a lower composition than what is noted. Although the preliminary screening of these materials has yielded promise of improving their electrochemical performance, further confirmation of the kinetic barrier to sodium reinsertion at high concentrations of sodium during discharge is required before further material engineering can be conducted to overcome this problem, such as particle size reduction or carbon coating the cathode active material particles. These potential solutions could prove key to improving the first-cycle coulombic efficiency of these materials by lowing the barrier for reentry of sodium into the structure at later stages of discharge. However, these experiments fall out of the primary scope of this study, which was to ensure that sodium doping into the MO_2 layer is possible for these materials and to screen their preliminary electrochemical performance for indication of suppression of sodium ordering and layered-layered structural transitions during cycling.

Conclusions

Na^+ and Fe^{3+} were successfully substituted for Ni^{2+} starting with the base material $Na_3Ni_2SbO_6$ in a series of compounds of the formula $Na_{3+x}Ni_{2-2x}Fe_xSbO_6$ ($0 \leqslant x \leqslant 0.5$). The goal of executing this doping strategy was to obtain a 3d transition-metal layered oxide with sodium occupation in the MO_2 layer of the material to suppress Na^+ ordering in the interlayer space and layered-layered phase transitions during cycling, which are the biggest problems hindering the practical application of layered sodium cathodes. This strategy was successful as the cyclic voltammograms and voltage vs composition curves for these materials showed a gradual dissipation of distinct $Ni^{2+}/^{3+}$ and $Ni^{3+/4+}$ redox reactions at particular voltages; instead, a single smooth voltage curve emerged for compositions $x \geqslant 0.3$, which is reminiscent of the voltage profile for commercial lithium layered oxide cathodes. An ex situ X-ray diffraction study revealed that the O3 → O3 + P3 → P3 → P3 + O1 → O1 layer transitions that occur during charge to 4.0 V vs Na^+/Na for the base $Na_3Ni_2SbO_6$ material are limited to no more than a transition to a final P3 layer stacking when charged up to 4.3 V vs Na^+/Na for the $Na_{3.3}Ni_{1.4}Fe_{0.3}SbO_6$, the earliest material in the series to display only a single voltage plateau in the voltage vs composition curve.

For this series of materials, a low first-cycle coulombic efficiency is observed that is attributed to a kinetic barrier that limits the amount of sodium that can be reinserted into the materials on first discharge to fully reform the O'3-layered phase of the pristine materials. This hypothesis is consistent with the reported electrochemical characteristics of the structurally analogous O'3-layered $Na_3Ni_{1.5}TeO_6$. Sodium ordering and layer-layer phase transitions were successfully suppressed in these materials through the tailoring of the material composition, but their cyclability can be further improved through the active particle engineering to circumvent this kinetic barrier limiting the first-cycle efficiency of these materials. The insights gleaned from this study can be used to further the development of layered Na_xMO_2 oxides towards a commercially viable sodium cathode material as sodium substitution in the MO_2 layer remains a viable strategy for mitigating the negative effects of the structural nuances of these materials, but further research is required to tailor the material compositions towards a truly competitive material.

Acknowledgments

NMR spectra were collected on a Bruker Avance III HD 400 MHz spectrometer funded by NSF grant CHE-1626211. The authors acknowledge Steve Sorey for his assistance during NMR data acquisition. We appreciate the computing resources provided by the Texas Advanced Computing Center (TACC) and the National Energy Research Scientific Computing Center. Hadi Khani and Nicholas S. Grundish acknowledge Companhia Brasileira de Metalurgia e Mineração (CBMM) for their financial support.

ORCID

Hailong Lyu https://orcid.org/0000-0002-2211-2148
Hadi Khani https://orcid.org/0000-0002-4023-5504

References

1. C. Delmas, *Adv. Energy Mater.*, **8**, 1703137 (2018).
2. J. Ma et al., *J. Phys. D: Appl. Phys.*, **54**, 183001 (2021).
3. C. Delmas, D. Carlier, and M. Guignard, *Adv. Energy Mater.*, **11**, 2001201 (2021).
4. L. Vitoux, M. Guignard, M. R. Suchomel, J. C. Pramudita, N. Sharma, and C. Delmas, *Chem. Mater.*, **29**, 7243 (2017).
5. D. Yuan, X. Liang, L. Wu, Y. Cao, X. Ai, J. Feng, and H. Yang, *Adv. Mater.*, **26**, 6301 (2014).
6. F. Aguesse, J.-M. Lopez del Amo, L. Otaegui, E. Goikolea, T. Rojo, and G. Singh, *J. Power Sources*, **336**, 186 (2016).
7. Y. Kee, N. Dimov, A. Staykov, and S. Okada, *Mater. Lett.*, **183**, 187 (2016).

8. J. Ma, S.-H. Bo, L. Wu, Y. Zhu, C. P. Grey, and P. G. Khalifah, *Chem. Mater.*, **27**, 2387 (2015).
9. N. S. Grundish, I. D. Seymour, Y. Li, J.-B. Sand, G. Henkelman, C. Delmas, and J. B. Goodenough, *Chem. Mater.*, **32**, 10035 (2020).
10. J. Zhao, L. Zhao, N. Dimov, S. Okada, and T. Nishida, *J. Electrochem. Soc.*, **160**, A3077 (2013).
11. B. Mortemard de Boisse, D. Carlier, M. Guignard, E. Guerin, M. Duttine, A. Wattiaux, and C. Delmas, *Chem. Mater.*, **30**, 7672 (2018).
12. V. V. Politaev and V. B. Nalbandyan, *Solid State Sci.*, **11**, 144 (2009).
13. K. Momma and F. Izumi, *J. Appl. Crystallogr.*, **44**, 1272 (2011).
14. I. Hung, L. Zhou, F. Pourpoint, C. P. Grey, and Z. Gan, *JACS*, **134**, 1898 (2012).
15. D. Massiot, F. Fayon, M. Capron, I. King, S. Le Calvé, B. Alonso, J.-O. Durand, B. Bujoli, Z. Gan, and G. Hoatson, *Magn. Reson. Chem.*, **40**, 70 (2002).
16. G. Kresse and J. Furthmüller, *Physical Review B*, **54**, 11169 (1996).
17. P. E. Blöchl, *Physical Review B*, **50**, 17953 (1994).
18. J. P. Perdew, K. Burke, and M. Ernzerhof, *Phys. Rev. Lett.*, **77**, 3865 (1996).
19. V. I. Anisimov, J. Zaanen, and O. K. Andersen, *Physical Review B*, **44**, 943 (1991).
20. S. L. Dudarev, G. A. Botton, S. Y. Savrasov, C. J. Humphreys, and A. P. Sutton, *Physical Review B*, **57**, 1505 (1998).
21. F. Zhou, M. Cococcioni, C. A. Marianetti, D. Morgan, and G. Ceder, *Physical Review B*, **70**, 235121 (2004).
22. J. Kim, D. S. Middlemiss, N. A. Chernova, B. Y. X. Zhu, C. Masquelier, and C. P. Grey, *JACS*, **132**, 16825 (2010).
23. D. S. Middlemiss, A. J. Ilott, R. J. Clément, F. C. Strobridge, and C. P. Grey, *Chem. Mater.*, **25**, 1723 (2013).
24. E. A. Zvereva et al., *Physical Review B*, **92**, 144401 (2015).
25. C. Delmas, C. Fouassier, and P. Hagenmuller, *Physica B + C*, **99**, 81 (1980).
26. Z. Yang, Y. Jiang, L. Deng, T. Wang, S. Chen, and Y. Huang, *J. Power Sources*, **360**, 319 (2017).
27. M. Tamaru, X. Wang, M. Okubo, and A. Yamada, *Electrochem. Commun.*, **33**, 23 (2013).
28. D. Carlier, M. Ménétrier, C. P. Grey, C. Delmas, and G. Ceder, *Physical Review B*, **67**, 174103 (2003).
29. R. J. Clément, P. G. Bruce, and C. P. Grey, *J. Electrochem. Soc.*, **162**, A2589 (2015).
30. K. Märker, P. J. Reeves, C. Xu, K. J. Griffith, and C. P. Grey, *Chem. Mater.*, **31**, 2545 (2019).
31. N. M. Trease et al., *Chem. Mater.*, **28**, 8170 (2016).
32. M. Sathiya, K. Ramesha, G. Rousse, D. Foix, D. Gonbeau, K. Guruprakash, A. S. Prakash, M. L. Doublet, and J. M. Tarascon, *Chem. Commun.*, **49**, 11376 (2013).
33. N. S. Grundish, I. D. Seymour, G. Henkelman, and J. B. Goodenough, *Chem. Mater.*, **31**, 9379 (2019).
34. A. Manthiram and J. B. Goodenough, *J. Solid State Chem.*, **71**, 349 (1987).
35. A. K. Padhi, K. S. Nanjundaswamy, C. Masquelier, S. Okada, and J. B. Goodenough, *J. Electrochem. Soc.*, **144**, 1609 (1997).
36. A. A. Pospelov and V. B. Nalbandyan, *J. Solid State Chem.*, **184**, 1043 (2011).